Zhu, F., Dai, D., & Yuan, Z. (2025). Resistance experiments on ships in a leader-follower formation. Physics of Fluids, 37(2), Article 023605. https://doi.org/10.1063/5.0249171.

Resistance experiments on ships in a leader-follower formation

Fengshen Zhu (朱风绅), Saishuai Dai (戴赛帅), Zhi-Ming Yuan* (元志明)
Department of Naval Architecture, Ocean & Marine Engineering, University of Strathclyde, Glasgow, G4 0LZ, UK

Abstract

The interaction between two ships in a leader-follower formation involves interference by both waves and viscosity, making the phenomenon highly complex. A series of experiments are conducted in this study to measure the total resistance of ships moving individually and in two-ship formations on calm water. The results indicate that the shape of the bow has a more significant impact on the total resistance of single ships than the shape of the stern. Specifically, the total resistance of a single ship with a transom stern is nearly identical to that of a ship with a sharp stern. However, ships with a flat bow exhibit significantly higher total resistance compared to those with a sharp bow. In a two-ship single-file formation, the hydrostatic drag of both the leading and trailing ships is significantly reduced when the gap between the two ships is small. This reduction occurs because the hollow in the water aft the transom stern induced by flow separation is filled by the bow waves of the trailing ship. When the trailing ship is positioned in the divergent-wave zone within the wake of the leading ship, wave interference between the two ships becomes the dominant factor influencing the variation in the total resistance of the trailing ship. As the gap between the two ships increases further, the wave interference weakens; however, the trailing ship still experiences a substantial reduction in resistance due to weakened flow separation and bubble drag reduction within the turbulent-bubble mixed flow region.

Keywords: single-file formation; wave interference; viscous interference; flow separation; bubble drag reduction.

1 Introduction

As global demand for resources continues to grow, the exploitation and utilization of marine resources have become increasingly essential, especially as land-based resources become more limited. This shift has led to a surge in maritime activities, requiring innovative approaches to enhance the efficiency and sustainability of ship operations, and reduce the carbon emissions. One promising approach is the strategic formation of ships, which can significantly reduce hydrodynamic resistance, thereby decreasing fuel consumption and environmental impact. The phenomenon of ducklings following their mother in a single-file formation was explained by Yuan et al.[1] through the mechanisms of wave-riding and wave-passing. By analyzing wave drag and wave patterns generated by ships in various single-file formations, Zhu and Yuan[2] further generalized and extended these mechanisms, providing deeper insights into their application in naval architecture.

A comprehensive understanding of the mutual interference between ships, encompassing not only wave interference but also the effects induced by fluid viscosity, is critically

* Corresponding author email: zhiming.yuan@strath.ac.uk

important for advancing the study of drag reduction in ship formations. To date, numerous researchers have devoted extensive efforts to the numerical calculations and experimental measurements of the drag components in both single and multi-hull ships. Based on the thin-ship approximation, Michell[3] derived the wave resistance of a ship moving at a steady speed in calm water. The Michell integral was further adopted to predict the wave drag of multi-hull ships by combining different techniques. Hsiung[4] expressed the wave resistance of catamarans in quadratic form by introducing a set of “tent” functions. Suzuki et al.[5] determined the optimal positions of trimaran outriggers by mathematically representing the hull form with cosine waterlines and parabolic frame lines. In the experimental tests, the Longitudinal-Cut Method (LCM) was extensively investigated to measure the wave resistance by analyzing the wave profile parallel to the model's velocity[6-11]. Additionally, the transverse-cut method was achieved by researchers[12, 13] in numerical simulations. Several correlation lines[14-16] have been formulated to predict the frictional resistance of a smooth plate. The correction line proposed by ITTC 1957[17] is commonly adopted in calculating the frictional resistance of a vessel. For a ship with a three-dimensional shape, the form resistance is associated with frictional resistance, viscous pressure resistance, and flow separation[18]. The form factor method was first proposed by Hughes[19], in which the total resistance is the sum of the form resistance and the residual resistance. This method was later improved by ITTC 1978[20], considering the contributions of roughness allowance and air resistance.

The transom stern is a popular hull form design, especially in high-speed vessels. However, the wake behind the transom stern is complex, which poses challenges for the prediction of ship resistance. Earlier studies primarily focused on the macroscopic characteristics of the wake. Flow separation at the transom stern can generate partial or complete ventilation, resulting in a hollow cavity on the free surface. A wet or dry transom stern leads to hydrostatic drag due to the absence of hydrostatic pressure on the transom surface. To estimate this hydrostatic drag, Doctors et al.[21-25] proposed two sets of regression formulas based on extensive experiments to predict the drop in the water level and the length of the hollow cavity behind the transom. A typical technique for handling transom flow in numerical simulations is to impose the Kutta condition at the trailing edge, ensuring a smooth detachment of the wave flow from the stern[26-28]. With improvements in computational methods and experimental techniques, significant effort has been devoted to studying the microscopic characteristics of the wake behind the transom stern. The closure of the hollow or the reattachment of the flow is usually accompanied by wave breaking, air entrainment and spray generation, leading to significant energy dissipation and increased resistance. The overturning and breaking of the free surface cause air entrainment, which further generates bubble plumes or bubble clouds. Hendrickson et al.[29] analyzed the flow structures in the air-water mixed region and the characteristics of air entrainment behind rectangular dry transom sterns using the Lagrangian cavity identification technique and high-resolution Implicit Large Eddy Simulation (ILES). They also characterized the Incompressible Highly Variable Density Turbulence (IHVDT) in the mixed-phase region by developing an explicit algebraic closure model for the Turbulent Mass Flux (TMF)[30]. Terrill and Taylor[31] measured the void fraction field by deploying a conductivity probe vertical array at the blunt transom of a full-scale surface ship. Using optical laser beam scattering characteristics, Abbaszadeh et al.[32] presented the average bubble size and bubble number density distribution in the wake of a transom stern model.

Air lubrication technique is one of the trending methods to reduce the frictional resistance of marine vehicles. Based on different working principles, it can be classified into three types of drag reduction: Bubble Drag Reduction (BDR), Air Layer Drag Reduction (ALDR), and Air Cavity Drag Reduction (ACDR)[33]. The BDR method can be achieved by injecting microbubbles into the Turbulent Boundary Layer (TBL), which influences the turbulent transport of momentum[34]. Laser Doppler velocimeter measurements by Kato et al.[35] in a turbulent boundary layer with microbubbles demonstrated a decrease in near-wall velocity and velocity gradient, resulting in reduced shear stress. Hassen et al.[36, 37] employed particle tracking velocimetry to measure the velocity fields of horizontal channel flow, finding that microbubble injection into a turbulent boundary layer can achieve up to 40% drag reduction by dynamically interacting with the turbulence structure and altering the vorticity and viscous sublayer thickness. A hydrofoil bubble generator, developed by Kumagai et al.[38] and Murai et al.[39], achieved a net power saving of 5–15% when introduced to the ship hull in a series of full-scale tests. When sufficient bubbles are injected beneath the flat bottom of a ship, they may coalesce to form an air layer. A complete replacement of the liquid phase with the air phase within the boundary layer nearly eliminates all friction drag. Friction drag reduction exceeding 80% can be achieved when bubbles form a thin, stable, continuous gas film beneath the surface of a long flat plate at the lowest inflow speed and highest air injection rate[40, 41]. However, ALDR is sensitive to inflow conditions; at high flow speeds, the air layer becomes unstable and fragile. The ACDR method can mitigate this disadvantage by modifying the hull design, particularly through the use of stepped hulls on planning crafts. Lay et al.[42] examined the ventilated cavity flow formed downstream of a backward-facing step and found that stable cavities were produced, reducing skin drag by more than 95%.

In addition to utilizing wave interference to reduce drag, the trailing ship may exploit other interferences, such as bubbles or turbulence flow in the wake of the leading ship, to save energy. Motivated by these interesting phenomena, some critical questions are raised:

- Can we quantify the contributions of wave interference and viscous interference to the total drag reduction?
- How much drag reduction in total can be achieved for formations with different configurations when considering the viscous effect?
- Does the transom stern design more effectively contribute to drag reduction in ship formations compared to other stern designs?
- What role does the bubble flow generated by a leading ship play in reducing the drag of a trailing ship?

In this paper, wave and viscous interferences in a leader-follower formation are investigated through a series of experimental tests. The resistance components of each ship in the formation are determined using the form factor method. Furthermore, the total resistance of three different ship models is compared, and the resistance components of one particular model are analyzed with the aid of the in-house code MHydro and the ITTC 1957 correction line[43]. The complex interference between ships is finally revealed by examining three formations with different configurations, identifying three critical zones in the wake of the leading ship.

2 Estimation of resistance components

2.1 Resistance components of a single ship

According to the ITTC 1978[44], the total resistance of a single ship moving steadily in calm water can be expressed by

$$C_T^s = (1 + k) \cdot C_F + C_W + \Delta C_F + C_{AA} \tag{1}$$

where C_T^s is the total resistance coefficient, $(1+k)$ is the form factor, C_F is the frictional resistance coefficient, ΔC_F is the frictional resistance coefficient caused by roughness, C_{AA} is the air resistance coefficient. In the experiment, the ship surface is smooth, thereby ΔC_F is assumed to be zero. The air resistance is also negligible, thus the total resistance can be simplified into

$$C_T^s = (1+k)\cdot C_F + C_W \tag{2}$$

The frictional resistance coefficient C_F can be obtained using ITTC 1957 correction line[43]

$$C_F = \frac{0.075}{(logRe-2)^2} \tag{3}$$

where Re is the Reynolds number, defined as

$$Re = \frac{UL}{\nu} \tag{4}$$

in which U is the movement speed, L is the ship length, ν is the kinematic viscosity of the water.

When the ship moves at very low speeds, the wave-making resistance becomes negligible. Thus, the form factor can be calculated by:

$$1+k = \lim_{F_r\to\infty}\frac{C_T^s}{C_F} \tag{5}$$

The form factor is independent of the scale effect and moving speed[44]. Even though some researchers have challenged this point[45], the method is still adopted in our study.

2.2 Resistance components of ship formations

The resistance components in a single-file formation are more complicated than those of single ships. Insel [46] conducted an in-depth analysis of the resistance components of high-speed displacement catamarans, which is helpful for the investigation of ships arranged in a single-file formation. The interaction effect can be divided into two parts:

1) Viscous interference: The bow waves generated by the trailing ship induce variations in the perturbation velocity field behind the leading ship, consequently modifying the form factor. Furthermore, as the waves from one vessel propagate to another, the wetted surface area changes, subsequently affecting the skin frictional resistance. The turbulence and air bubbles in the wake of the leading ship could also affect the frictional resistance of the trailing ship.
2) Wave interference: The superposition or cancellation of waves generated by the two ships can result in constructive or destructive interference, significantly impacting the wave resistance experienced by each vessel.

Taking the interference effects into account, the total resistance of the *n*-th ship in a formation can be expressed by

$$C_T^n = (1+\alpha k)\cdot \beta C_F + \gamma C_W \tag{6}$$

where α is the form resistance interference factor, β is the frictional resistance interference factor, and γ is the wave resistance interference factor.

Generally, "drag" is commonly used in studies involving animals and aerodynamics, while "resistance" is more frequently employed in ship design and naval architecture. Since the term "wave drag reduction" has been adopted in previous studies[1, 2], "total drag reduction" is retained in this paper for consistency. Based on the definition of the wave drag reduction[2], the total drag reduction coefficient on the *n*-th ship in a formation is defined as:

$$C_{DR}^{T} = \left(1 - \frac{C_T^n}{C_T^s}\right) \times 100\%, n = 0 \; and \; 1 \tag{7}$$

where C_T^s is the total drag of a single ship, either the leading one or the trailing one, moving solely in clam water. Obviously, $C_{DR}^{T} > 0$ indicates the total resistance is reduced in a formation due to the hydrodynamic interaction; whilst $C_{DR}^{T} < 0$ represents an increase in total resistance. No interaction is found at $C_{DR}^{T} = 0$, and the total resistance is the same as that of independent moving. Here, *n* denotes the number of ships in the formation, and *n* = 0 and 1 denote the leading and trailing ship, respectively.

3 Experimental set-up

A series of resistance tests were conducted in the towing tank at the Kelvin Hydrodynamics Laboratory (KHL), University of Strathclyde. The main dimensions of the tank are 76 m in length, 4.6 m in width, and 2 m in depth, respectively. The flap-type wavemaker is installed at one end of the tank, while the sloping beach is located at the other end to absorb the waves. In the experimental tests, the ship models were towed by a carriage equipped with a computer-controlled digital drive system, achieving a maximum towing speed of 5 m/s.

Figure 1. Towing tank and the carriage in KHL.

The total resistance measurements were carried out using a three-axis CCDXYZ-250KGload cells, manufactured by Applied Measurements Ltd. The load cell was fixed at the Center of Gravity of the model at one end, and the other end of the load cell was rigidly connected to the carriage through a 90 mm by 90 mm extrusion as demonstrated by Figure 1. The leading ship model was securely fixed to the front of the carriage, while the trailing ship model was installed behind the leading one with aligned longitudinal centerlines. The trailing ship was fixed to a moveable sliding frame (see Figure 2 for illustration). The sliding frame only allows movement in the surge direction. Different separations between the two ships were achieved simply by sliding the frame forward and backwards. The sliding frame (hence the trailing ship) was locked in place upon a desired separation was achieved. In the experiment, both the leading and trailing ships were rigidly fixed, with no investigation into the effects of sinkage or trim motion.

Figure 2. Load cell mounted on the model and sliding frame for adjusting the trailing ship.

During the test, ship models were initially accelerated by the carriage, reaching stable constant designed towing speeds after roughly 5 seconds. On average, 20 seconds of constant speed measurements were achieved which provided sufficient data samples with a sampling frequency over 100Hz. An interval of 15 minutes was allocated between tests to allow for the dissipation of disturbances. During the tests, both total forces experienced by each ship model and the carriage speed were measured and recorded through a 16-bit data acquisition system. Subsequent data analysis and processing were conducted using the commercial software Spike.

Experimental uncertainties include bias uncertainties resulting from systematic inaccuracies and random uncertainties arising from individual measurement variations. In the present experiment, the bias uncertainty mainly originates from the load cell measurement, and it is accessed through load cell calibration. The random uncertainties caused by variation of water temperature, initial state of the water before each test are accessed through repeatability tests.

To investigate the fundamental principles, the ship models were simplified to minimize the impact introduced by ship designs (streamlined ship designs are optimised for resistance). Three distinct models were employed in the experiment, with their detailed parameters and shapes illustrated in Table 1. When measuring the total drag of a single ship, the models were towed in both directions.

Table 1. Main dimensions of different ship models (unit: m)

Components	mid-body	bow	stern

Shape	cuboid			right triangular prism		right triangular prism	
Parameters	length	width	draft	side	draft	side	draft
Model A	1	0.25	0.15				
Model B	1	0.25	0.15	0.25	0.15		
Model C	1	0.25	0.15	0.25	0.15	0.25	0.15

Three distinct ship formations were configured by incorporating various models, as illustrated in Figure 3. Configuration I integrates Model A and Model B， Configuration II comprises two instances of Model B, and Configuration III consists of two instances of Model C. Due to the adjustment range limitations of the sliding frame, the gap between the two models in Configuration I ranges from 0.1 m to 2.5 m. For Configuration II, the gap varies from 0.1m to 2.3 m, while for Configuration III, it extends from 0 m to 2 m. Given the intensification of interference between the two models at closer separation distances, the initial adjustment interval is set to 0.05 m. As the distance between the models increases, this interval is adjusted to 0.1 m or more. The maximum testing speed is limited to avoid the impact of “green water”. In ship formation tests, the movement speeds were set at 1.036 m/s, 1.209 m/s, 1.382 m/s, 1.554 m/s, 1.727 m/s, and 1.9 m/s, which correspond to Froude numbers of 0.3, 0.35, 0.4, 0.45, 0.5, and 0.55 for Model B, respectively.

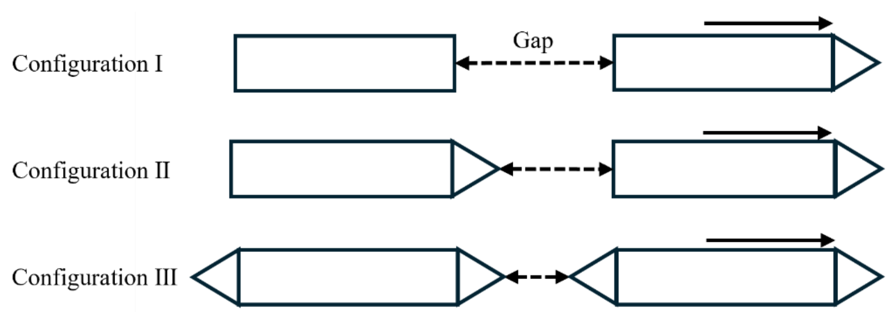

Figure 3. Different ship configurations.

4 Results and discussions

4.1 Resistance of a single ship

Understanding the wake field of a single ship with a transom stern is beneficial for analyzing the hydrodynamic interference between ships. As shown in Figure 4(a), when a ship moves in calm water, two sets of right-handed coordinate systems are employed. The first one is a global reference system, designated as *O-XYZ*. In this system, the positive *Z*-axis is pointing upwards and it remains stationary relative to the calm water surface. The second is a local reference system, denoted as *o-xyz*, which is fixed to the Center of Gravity of the model. The ship moves at a speed *U* along the negative *X*-axis. The wake field of a transom stern can be segmented into three distinct regions along the flow direction: the converging wave corner region, the rooster tail region, and the divergent wave region[29]. Figure 4(b) illustrates the wake filed of a ship with transom stern moving at 1.9 m/s. The flow separation behind the transom stern leads to stern ventilation, resulting in a nearly dry stern state. A hollow is observed behind the transom stern, with ridges rising from the lower corner. These ridges angle toward the stern centerline, entraining some air and generating significant spray. As the wake spreads laterally, the divergent wave train maintains a steady V-shape. Due to air entrainment and turbulent disturbance, a “whitewater zone” with numerous bubbles forms within the surrounding flow field[47].

Since the transom-draft Froude number was first proposed by Saunders[48] to quantify the transom ventilation, it has become a crucial parameter in the study of transom stern issues. The transom-draft Froude number is defined as

$$F_T = \frac{U}{\sqrt{gT_d}} \tag{8}$$

where T_d is the transom draft.

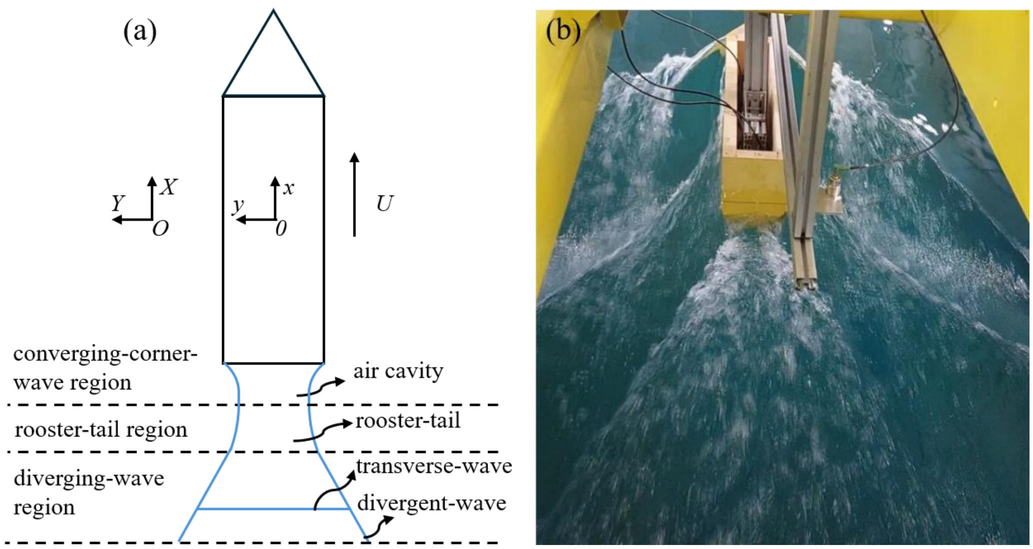

Figure 4. (a) Characteristics of the wake filed behind a transom stern. (b) The wake field of a ship with transom stern moving at 1.9 m/s.

Figure 5 illustrates the total resistance of various single ship models. To evaluate the uncertainty of resistance measurements, several speeds were tested two or three times for different models. The resistance results demonstrate good repeatability, and the differences are within acceptable limits. Due to the asymmetry in geometry, Model B exhibited a significant difference in total resistance when towed in opposite directions. The total resistance of Model A is nearly equivalent to that of Model B when operating in reverse at all speeds. Similarly, the total resistance of Model C closely aligns with that of Model B when moving forward. Both sets of models feature an identical bow design but differ in their stern configurations. Doctors[49] pointed out that the formation of a hollow behind the transom creates a virtual extension of the vessel’s length. This phenomenon is evident in the present experiments, where models with transom sterns, despite being shorter than those with sharp forms, demonstrate comparable hydrodynamic performance.

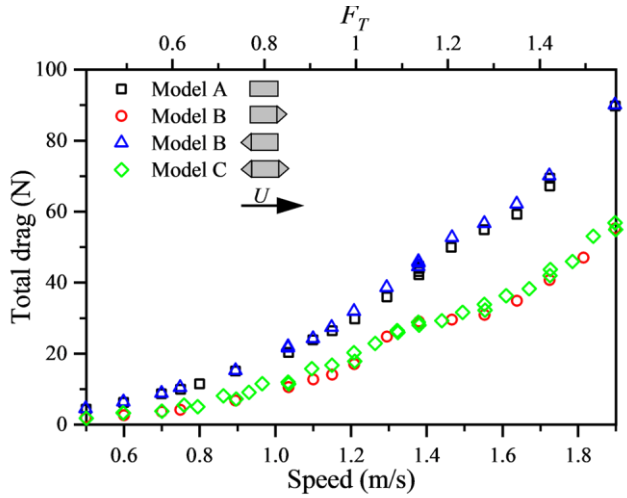

Figure 5. Total drag of various individual ship models.

The total drag of Models A and B in reverse is significantly higher than that of Models C and B moving forward, as shown in Figure 5. Models with a flat bow generate more frontal waves compared to those with a sharp bow, resulting in higher wave-making resistance, especially at high speeds. Due to the interference between waves generated by the bow and stern, a hump in the resistance is observed near 1.4 m/s for Models C and B moving forward. Figure 6(a) and (b) illustrate the wake fields associated with the peak and trough values of the total resistance. It is noted that when the ship travels at a speed of 1.382 m/s, a constructive wave interference takes place between the waves generated by the bow and the stern, as shown in the red dashed area of Figure 6(a). The ship nearly rides two wavelength and there is no phase difference between waves generated by the bow and the stern. Consequently, the wave amplitude behind the transom stern is significantly amplified. Additionally, the divergent waves are hardly influenced by the bow waves, and the divergent wave angle behind the transom stern closely matches that of the bow-generated waves. In contrast, at a speed of 1.554 m/s, destructive interference occurs between the bow and stern waves, as shown in the red dashed region of Figure 6(b). The bow waves significantly disrupt the divergent waves behind the transom stern, leading to a reduction in both the divergent wave angle and wave amplitude. However, this effect is insignificant for Models A and B in reverse. The stagnation pressure at the forebody hull is significantly higher for models with a flat bow compared to those with a sharp bow. Consequently, the hydrostatic drag is also greater for models with a flat bow than for those with a sharp bow. The variation caused by wave interference between the bow and stern may be negligible compared to the substantial hydrostatic drag for models with a flat bow.

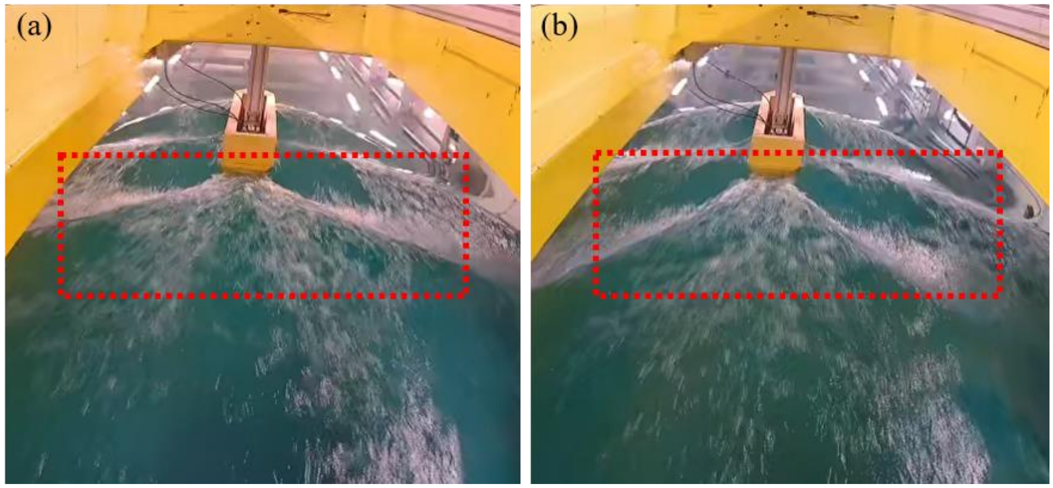

Figure 6. Comparison of the wake field for a ship traveling at (a) 1.382 m/s and (b) 1.554 m/s.

Figure 7 illustrates the total drag and its individual components for Model C. The frictional resistance can be calculated by

$$R_F = \frac{1}{2}\rho S U^2 C_F \tag{9}$$

where S is the wetted body surface area and ρ is the water density. The form factor is determined using formulation (5), with C_T and C_F substituted by by R_T and R_F, where R_T is the measured total resistance. Based on the drag data obtained at 0.597 m/s and 0.699 m/s, a form factor of 4 is obtained. This value is much higher than that of streamlined vessels, primarily due to the intensive flow separation caused by its sharp cross-section.

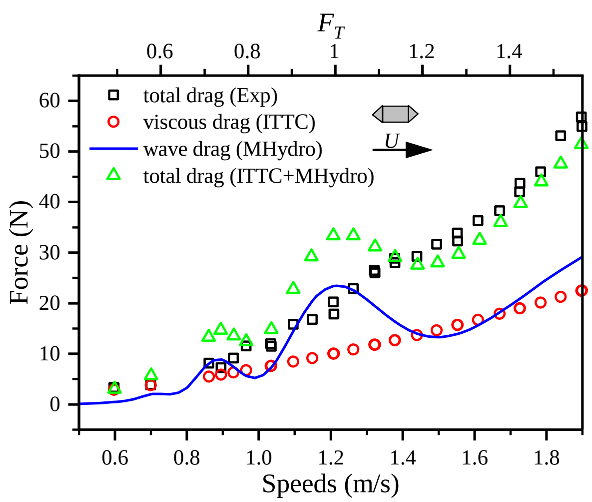

Figure 7. Total drag and individual drag components of Model C.

An in-house code MHydro[50] is employed to predict the wave drag of Model C. As shown in Figure 7, the total drag predicted by both the MHydro and ITTC formulas closely aligns with experimental measurements, particularly at higher speeds. When moving speed is below 0.8 m/s, the wave drag is consistently lower than the drag due to viscosity, which includes both frictional and form drag. Afterwards, they are at the same level, and in some velocity regions, wave drag is higher than viscous drag. The wave drag is observed to exceed the total drag at approximately 1.2 m/s, which is not reasonable. The wave drag is calculated by integrating the pressure over the wet surface within the framework of linear potential flow theory. However, the impact of nonlinear waves and flow separation on the prediction of wave drag cannot be ignored in this study, which could lead to the discrepancy.

4.2 Resistance of ships with different configurations

In configuration tests, results were obtained by towing the ships only in forward direction and Configuration II is selected as the base group. When compared with Configuration I, both configurations feature the same leading ship, with a sharp bow and transom stern. However, the bow of the trailing ship with a transom stern differs: Configuration I features a flat bow, while Configuration II has a sharp bow. In comparison with Configuration III, both configurations have identical leading and trailing ships, but Configuration II uses ships with a sharp bow and transom stern for both, whereas Configuration III adopts ships with a sharp bow and sharp stern. The gap between the two ships in each configuration is dimensionless, expressed as the ratio of the gap length (G) to the length of Model A (L_0), denoted as G/L_0.

4.2.1 Comparison between Configuration I and II

Figure 8 illustrates the reduction in total drag for each ship in Configuration I and II across various speeds. When the gap G/L_0 is less than 0.5, the C_{DR}^{T} values for both the leading and trailing ships in Configuration I are generally higher than those in Configuration II. Especially, the trailing ship in Configuration I consistently achieves a significant total drag reduction, reaching approximately 70% at most speeds when the gap is very small. As the gap G/L_0 widens from 0.1 to 0.5, the C_{DR}^{T} values for the leading ship in Configuration II decrease more significantly than those in Configuration I. On one hand, the trailing ship with a flat bow in Configuration I generates more frontal waves compared to the trailing ship with a sharp bow in Configuration II. These waves can fill the cavity behind the transom stern of the leading ship, significantly decreasing the hydrostatic drag of the leading ship. On the other hand, a flat bow more effectively prevents cross flow from concentrating at the centre, thereby avoiding wave overturning and breaking. Additionally, it better utilizes the low-pressure area in the cavity region to reduce the stagnation pressure on the bow surface compared to a sharp bow.

The turning point of the C_{DR}^{T} values for the trailing ship in Configuration II is observed when G/L_0 is approximately 0.5. At this point, the bow of the trailing ship enters the high-pressure zone in the rooster tail region of the leading ship, which is unfavourable for drag reduction. However, this effect is insignificant for the trailing ship in Configuration I, as the bow waves from the trailing ship prevented the formation of the rooster tail. Figure 9(a) illustrates the wave field of Configuration II when the ships travel at a speed of 1.9 m/s with G/L_0 = 0.5. It is clear that the bow of the trailing ship is precisely positioned within the rooster tail region, where significant spray occurs due to the closure of the air cavity, resulting in a high-pressure zone. In Configuration II, the bow waves produced by the trailing ship are relatively weak and fail to disrupt the high-pressure rooster tail effectively. In contrast, as shown in Figure 9(b), for Configuration I at a speed of 1.727 m/s with the same gap, the trailing ship with its flat bow generates stronger bow waves. These bow waves interfere with the closure of the air cavity flow, preventing the formation of the concentrated high-pressure rooster tail region. As a result, the adverse drag effect on the trailing ship is mitigated.

When the gap G/L_0 exceeds 0.5, the C_{DR}^{T} values for the trailing ship in Configuration II gradually increase, with wave interference beginning to dominate the interaction between the two ships in the diverging wave region of the leading ship. The wave interference between the two ships becomes more intensive as speed increases. At higher speeds, the wave amplitude increases significantly, resulting in the C_{DR}^{T} values of the trailing ship following a sinusoidal wave like pattern, as illustrated in Figure 8(e).

As the gap increases further, it becomes challenging for the leading ship to receive benefits from the interference, and the C_{DR}^{T} values for the leading ship in both configurations gradually approach zero. Simultaneously, the wave interference between the two ships weakens, and the C_{DR}^{T} values for the trailing ships in both configurations converge to constant values when G/L_0 exceeds 2 across various speeds. Within the turbulent-bubble mixed flow region, the drag reduction primarily arises from the decrease in form drag, as flow separation around the bow and behind the transom stern of the trailing ship is weakened when moving within the turbulent flow generated by the leading ship. This is analogous to the phenomenon where free-stream turbulence can shorten the separation bubble in a wind tunnel[51]. Additionally, drag reduction is also achieved through a decrease in skin friction. When the trailing ship moves within the bubble flow, the local average fluid density and relative flow velocity are both decreased compared to moving independently. The microbubbles may also enter the turbulent boundary layer near the hull surface, reducing the shear force.

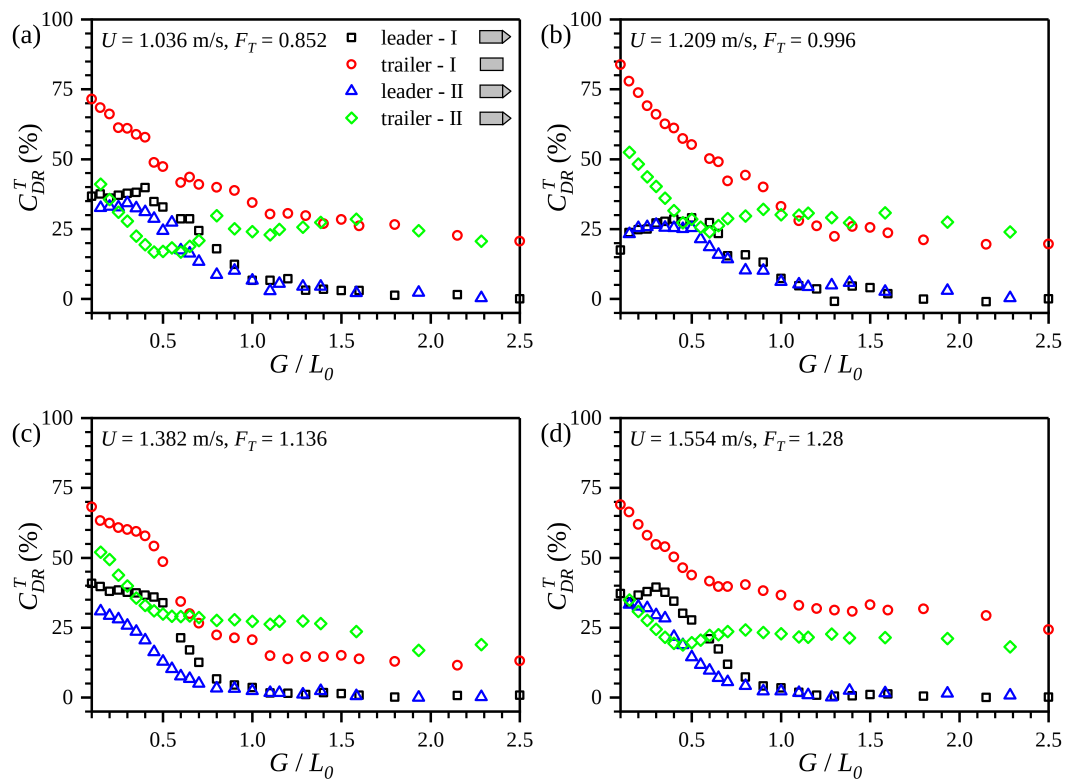

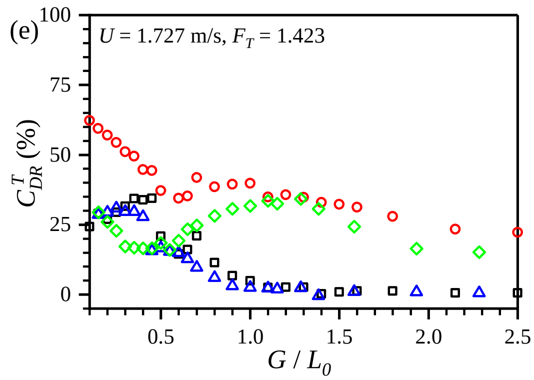

Figure 8. Comparison of total drag reduction between Configurations I and II. (a) 1.036 m/s; (b) 1.209 m/s; (c) 1.382 m/s; (d) 1.554 m/s; (e) 1.727 m/s.

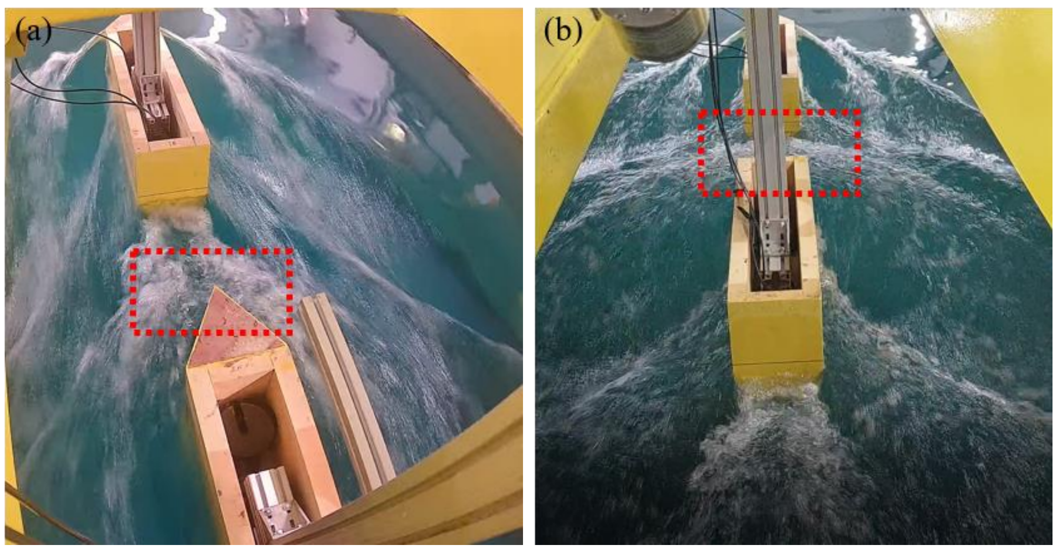

Figure 9. (a) Wave field for Configuration II with G/L_0 = 0.5 at a velocity of 1.9 m/s; (b) Wave field for Configuration I with G/L_0 = 0.5 at a velocity of 1.727 m/s.

4.2.2 Comparison between Configurations II and III

Figure 10 illustrates the reduction in total drag for ships in Configuration II and III at various speeds. When the gap G/L_0 is less than 0.5, the C_{DR}^{T} values for the leading ship in Configuration III are generally lower than those in Configuration II. Additionally, the C_{DR}^{T} values for the leading ship in Configuration III consistently decrease, while those in Configuration II remain nearly constant. At most speeds, the C_{DR}^{T} values for the trailing ship in Configuration III are also lower than those in Configuration II. The sharp stern can prevent the formation of cavities. Meanwhile, this design can induce the flow to concentrate towards the centre, generating a high-pressure region. Therefore, the transom stern design is more beneficial for total drag reduction compared to the sharp stern when G/L_0 is less than 0.5.

When the gap G/L_0 exceeds 0.5, the C_{DR}^{T} values for the leading ship in Configuration III decrease to zero earlier than those in Configuration II. Additionally, the trailing ships in Configuration III enter the wave-interference-dominated region earlier than those in

Configuration II. This occurs because the flow evolution in the wake of the leading vessel in Configuration III completes earlier due to the sharp stern. As illustrated in Figure 10(e), the C_{DR}^{T} trend of the trailing ship in Configuration III is significantly ahead of that in Configuration II.

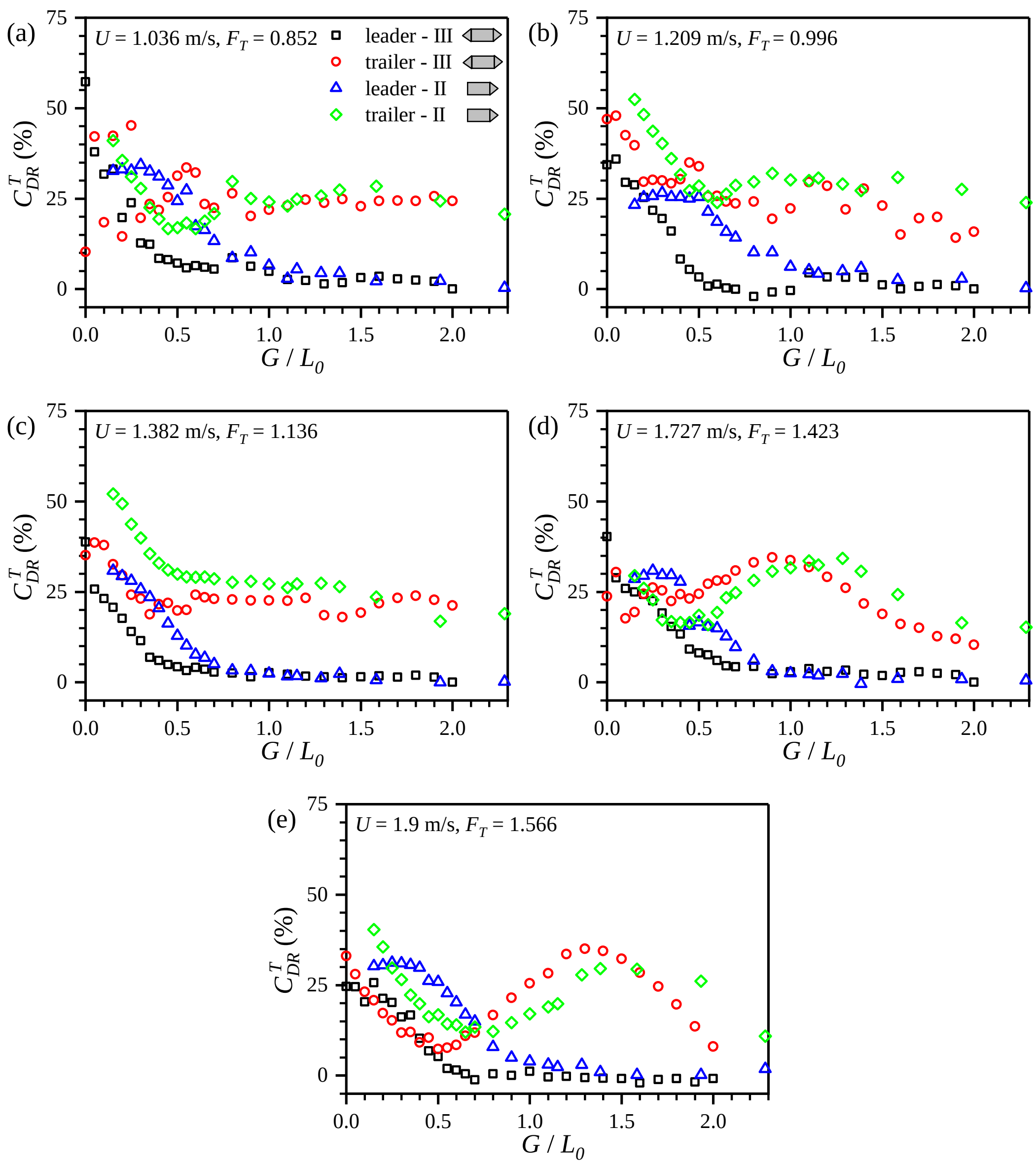

Figure 10. Comparison of total drag reduction between Configuration II and III. (a) 1.036 m/s; (b) 1.209 m/s; (c) 1.382 m/s; (d) 1.727 m/s; (e) 1.9 m/s.

Figure 11 illustrates the flow fields for three typical gaps at a speed of 1.554 m/s in configuration II. At G/L_0 = 0.15, both the leading and trailing ships experience reduced hydrostatic drag. The transom ventilation of the leading ship is nearly eliminated, and the frontal waves generated by the trailing ship are minimal. When the gap G/L_0 increases to 0.7, the trailing ship enters the divergent wave zone, benefiting from wave interference between the two ships and significantly contributing to total drag reduction. As the gap

G/L_0 widens to 1.6, wave interference weakens, making the reduction in form drag and frictional drag the dominant factor in the total drag reduction. These three positions represent different zones where the mechanisms contributing to total drag reduction vary. It should be noted that the lengths of these zones depend on the moving speed, so there are no absolute boundaries, especially for the length of the wave-interference-dominated zone.

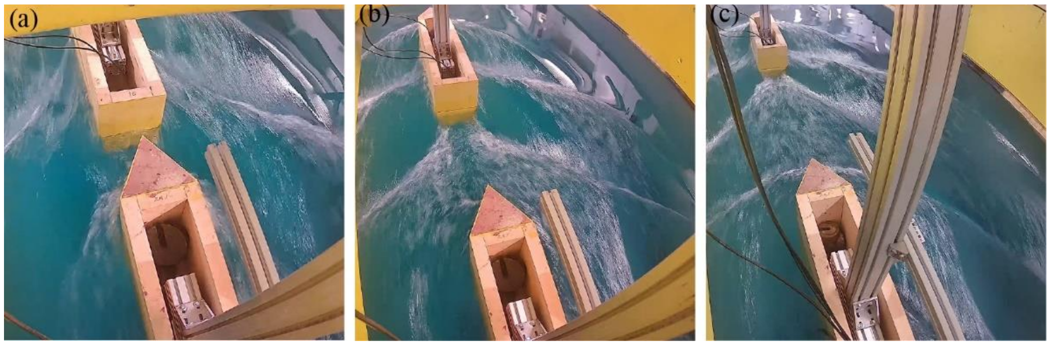

Figure 11. The flow fields of three different gaps in Configuration II when the velocity is 1.554 m/s. (a) G/L_0 = 0.15; (b) G/L_0 = 0.7; (c) G/L_0 = 1.6.

4.2.3 Comparison between total drag reduction and wave drag reduction

Figure 12 illustrates the reduction in total drag measured in experiments and the wave drag predicted by MHydro for each individual in Configuration III. When the gap G/L_0 is less than 0.5, the drag reduction values due to total interference for the leading ship are greater than those caused by wave interference alone. Additionally, as the gap widens, the wave drag reduction for the leading ship decreases more rapidly compared to the total drag reduction. Within potential flow theory, flow separation due to viscosity is not considered. In the real world, energy loss due to flow separation is unavoidable, especially for bluff bodies. In the experiments, the frontal waves generated by the trailing ship can not only reduce wave drag by offering a propulsion force for the leading ship but also help mitigate flow separation, thereby reducing viscous drag. When the gap G/L_0 exceeds 0.5, the wave interference C_{DR}^{T} (without viscous effect) of the leading ship is almost identical to the total C_{DR}^{T} (considering the viscous effect). This is because the frontal waves from the trailing ship can no longer reach the stern of the leading ship, making it challenging to alter the wave field around the leading ship.

The wave drag reduction values of the trailing ship oscillate around zero, while the total drag reduction values of the trailing ship oscillate around a positive value. Thus, the drag reduction due to viscous interference varies nearly linearly, with a slow decrease as the distance increases. This suggests that the trailing ship periodically benefits from wave interference while consistently gaining from viscous interference when moving in the turbulent flow of the leading ship. There is a phase difference between the total drag reduction and the wave drag reduction because the wave patterns are influenced by the turbulent disturbance, which further impacts the wave interference between the two ships.

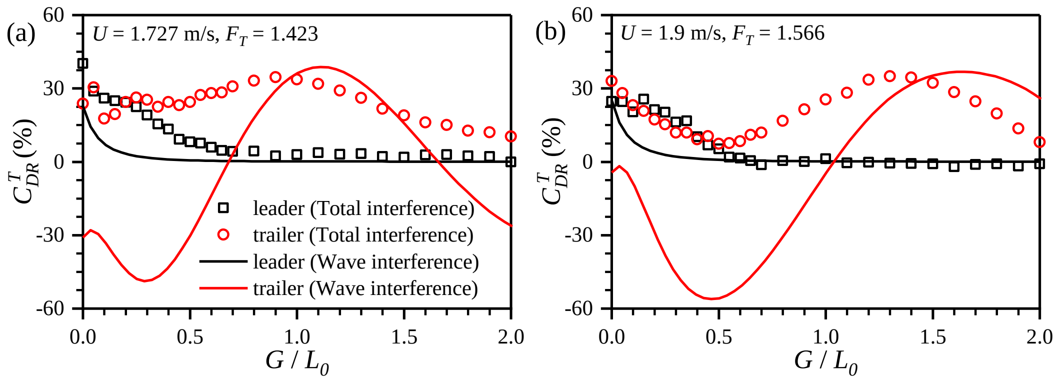

Figure 12. Comparison of total drag reduction between experimental and numerical results in Configuration III. (a) 1.727 m/s; (b) 1.9 m/s.

5 Conclusions

The total drag reduction of the ship formation benefits not only from wave interference but also from viscous interference. To fully understand the mechanism behind this total drag reduction in ship formations, resistance experiments are conducted on both single ships with different configurations and ship formations with various combinations. In the decomposition of the total drag, the form factor method is employed for the single ships and further extended to the ship formations. The ship form significantly influences its own flow field and, consequently, the flow fields of other ships in the formation. The flow separation of the transom stern is more intense than that of the sharp stern, thus the resistance of these two stern forms is examined. Additionally, the ship bows with flat and sharp forms are also considered in the tests. By comparing the resistance results and analysing the flow fields, the following conclusions are obtained:

1) For single ships with the same bows, there is little difference in total resistance between the transom stern and the sharp stern. This is because the flow separation behind the transom stern induces transom ventilation and the formation of an air hollow, which effectively elongates the ship's length.

2) The total resistance of a ship with a flat bow is significantly higher than that of a ship with a sharp bow, with the hydrostatic drag component being substantially greater for the flat bow, compared to the sharp bow.

3) The turbulent flow behind the transom stern is intense, leading to wave breaking and overturning, which induces air entrainment. The "whitewater" in the wake is observed due to the formation of air bubbles.

4) When two ships are in close proximity, a transom stern on the leading ship significantly aids in drag reduction for both vessels. The flow separation at the transom stern creates a low-pressure hollow. The bow waves from the trailing ship can fill this hollow, thereby reducing the hydrostatic drag of the leading ship. Simultaneously, the trailing ship benefits by releasing some of the high pressure on its bow surface, which also reduces its hydrostatic pressure resistance. For a trailing ship with a flat bow, the mutual benefit is more significant than with a sharp bow.

5) As the gap between two ships increases, the bow waves from the trailing ship hardly influence the leading ship, thus the leading ship receives significantly less

benefit. By contrast, the trailing ship enters the divergent wave zone in the wake of the leading ship, where wave interference significantly affects the total drag, especially at high speeds.

6) As the gap between the two ships continues to widen, the wave amplitude diminishes, making wave interference negligible. The wave drag reduction values of the trailing ship converge to a nearly constant value within the turbulent-bubble mixed flow region. This drag reduction can be attributed to two factors: the flow separation weakens when the trailing ship moves in the turbulent flow, reducing form resistance; and frictional resistance decreases as the trailing ship moves through the bubble flow, which alters the turbulent boundary layer on the hull surface, further reducing the viscous shear force.

It should be noted that in any zone, the reduction of resistance is a combination of three factors: flow separation, wave interference, and air lubrication. However, at different stages, one or two of these factors may dominate the total drag reduction. Further experiments are needed to quantify the contributions of both bubble drag reduction and the reduction due to turbulent flow. Additionally, the release of sinkage and trim motions may alter the resistance reduction effect, and related experiments will be conducted to investigate this further.

6 Data Availability

The data that support the findings of this study are available from the corresponding author upon reasonable request.

7 Reference

1. Z.-M. Yuan, M. Chen, L. Jia, C. Ji, andA. Incecik, "Wave-riding and wave-passing by ducklings in formation swimming," J. Fluid Mech. **928**, R2 (2021).

2. F. Zhu, andZ.-M. Yuan, "Wave drag and wave patterns by ships moving in a single-file formation," Phys. Fluids **36**, (2024).

3. J. H. Michell, "XI. The wave-resistance of a ship," The London, Edinburgh, and Dublin Philosophical Magazine and Journal of Science **45**, 106 (1898).

4. C.-C. Hsiung, "Optimal ship forms for minimum wave resistance," Journal of Ship Research **25**, 95 (1981).

5. K. Suzuki, andM. Ikehata, "Studies on minimization of wave making resistance for high speed trimaran with small outriggers," Journal of the Society of Naval Architects of Japan **1995**, 113 (1995).

6. J. N. Newman, *The determination of wave resistance from wave measurement along a parallel cut* (Ann Arbor, Michigan, USA, 1963).

7. K. Eggers, "An assessment of some experimental methods for determining the wavemaking characteristics of a ship form," Sname Transactions **75**, 112 (1967).

8. D. Moran, andL. Landweber, "A longitudinal-cut method for determining wavemaking resistance," Journal of Ship Research **16**, 21 (1972).

9. C.-E. Tsai, andL. Landweber, "Further Development of a Procedure for Determination of Wave Resistance from Longitudinal-Cut Surface-Profile Measurements," Journal of Ship Research **19**, 65 (1975).

10. F. Lalli, F. Di Felice, P. Esposito, A. Moriconi, andR. Piscopia, *Some remarks on the accuracy of wave resistance determination from wave measurements along a parallel cut* (Washington, DC, USA, 1998).

11. F. Lalli, F. Di Felice, P. Esposito, A. Moriconi, andR. Piscopia, "Longitudinal cut method revisited: A survey on main error sources," Journal of ship research **44**, 120 (2000).

12. D. E. Nakos, *Transverse wave cut analysis by a Rankine panel method* (Woods Hole, MA, USA, 1991).

13. H. Söding, "A method for accurate force calculations in potential flow," Ship Technology Research **40**, 176 (1993).

14. K. E. Schoenherr, "Resistance of flat surfaces moving through a fluid," Transactions of the Society of Naval Architects and Marine Engineers 279 (1932).

15. G. CWB, "A planar friction algorithm and its use in analysing hull resistance," Trans RINA (1999).

16. T. Katsui, *The proposal of a new friction line* (Osaka, Japan, 2005).

17. ITTC, *Report of Skin Friction and Turbulence simulation* (Madrid, Spain, 1957).

18. O. M. Faltinsen, *Hydrodynamics of High-Speed Marine Vehicles* (Cambridge University Press, Cambridge, 2006).

19. G. Hughes, "Friction and form resistance in turbulent flow, and a proposed formulation for use in model and ship correlation," RINA Transactions (1954).

20. ITTC, *Report of Performance Committee* (Hague, Netherlands, 1978).

21. L. Doctors, andR. Beck, *The separation of the flow past a transom stern* (2005).

22. K. J. Maki, L. J. Doctors, R. F. Beck, andA. W. Troesch, "Transom-stern flow for high-speed craft," Australian Journal of Mechanical Engineering **3**, 191 (2006).

23. L. J. Doctors, *Influence of the transom-hollow length on wave resistance* (Loughborough, UK, 2006).

24. L. J. Doctors, andU. o. N. S. Wales, "A numerical study of the resistance of transom-stern monohulls," Ship Technology Research **54**, 134 (2007).

25. K. J. Maki, L. J. Doctors, andR. Beck, *On the profile of the flow behind a transom stern* (Ann Arbor, Michigan, USA, 2007).

26. M. P. Tulin, andC. Hsu, "Theory of high-speed displacement ships with transom sterns," Journal of ship research **30**, 186 (1986).

27. D. E. Nakos, andP. Sclavounos, "Kelvin wakes and wave resistance of cruiser-and transom-stern ships," Journal of Ship Research **38**, 9 (1994).

28. A. Mola, L. Heltai, andA. DeSimone, "Wet and dry transom stern treatment for unsteady and nonlinear potential flow model for naval hydrodynamics simulations," Journal of Ship Research **61**, 1 (2017).

29. K. Hendrickson, G. D. Weymouth, X. Yu, andD. K.-P. Yue, "Wake behind a three-dimensional dry transom stern. Part 1. Flow structure and large-scale air entrainment," Journal of Fluid Mechanics **875**, 854 (2019).

30. K. Hendrickson, andD. K.-P. Yue, "Wake behind a three-dimensional dry transom stern. Part 2. Analysis and modelling of incompressible highly variable density turbulence," Journal of Fluid Mechanics **875**, 884 (2019).

31. E. J. Terrill, andG. R. Taylor, "Entrainment of air at the transoms of full-scale surface ships," Journal of Ship Research **59**, 49 (2015).

32. M. Abbaszadeh, M. M. Alishahi, andH. Emdad, "Experimental investigations on the bubbly wake of a transom stern model using optical laser beam scattering characteristics," Applied Ocean Research **104**, 102380 (2020).

33. S. L. Ceccio, "Friction drag reduction of external flows with bubble and gas injection," Annual Review of Fluid Mechanics **42**, 183 (2010).

34. X. Zhang, J. Wang, andD. Wan, "Euler–Lagrange study of bubble drag reduction in turbulent channel flow and boundary layer flow," Physics of Fluids **32**, (2020).

35. H. Kato, T. Iwashina, M. Miyanaga, andH. Yamaguchi, "Effect of microbubbles on the structure of turbulence in a turbulent boundary layer," Journal of Marine Science and Technology **4**, 155 (1999).

36. Y. A. Hassan, C. C. Gutierrez-Torres, andJ. A. Jimenez-Bernal, "Temporal correlation modification by microbubbles injection in a channel flow," International Communications in Heat and Mass Transfer **32**, 1009 (2005).

37. J. Ortiz-Villafuerte, andY. A. Hassan, "Investigation of microbubble boundary layer using particle tracking velocimetry," J. Fluids Eng. **128**, 507 (2005).

38. I. Kumagai, Y. Takahashi, andY. Murai, "Power-saving device for air bubble generation using a hydrofoil to reduce ship drag: Theory, experiments, and application to ships," Ocean Engineering **95**, 183 (2015).

39. Y. Murai, H. Sakamaki, I. Kumagai, H. J. Park, andY. Tasaka, "Mechanism and performance of a hydrofoil bubble generator utilized for bubbly drag reduction ships," Ocean Engineering **216**, 108085 (2020).

40. W. C. Sanders, E. S. Winkel, D. R. Dowling, M. Perlin, andS. L. Ceccio, "Bubble friction drag reduction in a high-Reynolds-number flat-plate turbulent boundary layer," Journal of Fluid Mechanics **552**, 353 (2006).

41. B. R. Elbing, E. S. Winkel, K. A. Lay, S. L. Ceccio, D. R. Dowling, andM. Perlin, "Bubble-induced skin-friction drag reduction and the abrupt transition to air-layer drag reduction," Journal of Fluid Mechanics **612**, 201 (2008).

42. K. A. Lay, R. Yakushiji, S. Makiharju, M. Perlin, andS. L. Ceccio, "Partial cavity drag reduction at high Reynolds numbers," Journal of Ship Research **54**, 109 (2010).

43. ITTC, *Report of Skin Friction and Turbulence simulation* (Proceeding of the 8th International Towing Tank Conference, 1957).

44. ITTC, *Report of Performance Committee* (Proceeding of the 15th International Towing Tank Conference, 1978).

45. K.-S. Min, andS.-H. Kang, "Study on the form factor and full-scale ship resistance prediction method," Journal of marine science and technology **15**, 108 (2010).

46. M. Insel, "An investigation into the resistance components of high speed displacement catamarans," University of Southampton, 1990.

47. S. Chen, T. Su, H. Guo, Y. Zhang, andH. Zou, "Study of “whitewater zone” optical properties in ship wake," Ocean Engineering **297**, 117060 (2024).

48. H. E. Saunders, *Hydrodynamics in Ship Design* (Society of Naval Architects and Marine Engineers, SNAME, 1957).

49. L. J. Doctors, *On the great trimaran-catamaran debate* (Seattle, Washington, USA, 1999).

50. Z.-M. Yuan, P. Kellet, A. Incecik, O. Turan, andE. Boulougouris, "Ship-to-ship interaction during overtaking operation in shallow water," Journal of Ship Research **59**, 172 (2015).

51. Y. Nakamura, andS. Ozono, "The effects of turbulence on a separated and reattaching flow," Journal of Fluid Mechanics **178**, 477 (1987).

Acknowledgments: Results were obtained using the ARCHIE-WeSt High Performance Computer (www.archie-west.ac.uk) based at the University of Strathclyde.